JGR Space Physics

RESEARCH ARTICLE
10.1029/2020JA028154

Reflected Protons in the Lunar Wake and Their Effects on Wake Potentials

Shaosui Xu[1], Andrew R. Poppe[1], Jasper S. Halekas[2], and Yuki Harada[3]

[1]Space Sciences Laboratory, University of California, Berkeley, CA, USA, [2]Department of Physics and Astronomy, University of Iowa, Iowa City, IA, USA, [3]Department of Geophysics, Kyoto University, Kyoto, Japan

Key Points:

- Reflected protons (RPs) have peak occurrence rates of ~20% downstream of the Moon in the lunar wake at $N \times 2\pi R_g$
- We infer a nonmonotonic field-aligned potential structure in the presence of reflected protons in the wake for the first time
- When RP density is above ~30% of local solar wind proton density, the wake potential scales as the logarithmic density of RPs

Correspondence to:
S. Xu,
shaosui.xu@ssl.berkeley.edu

Citation:
Xu, S., Poppe, A. R., Halekas, J. S., & Harada, Y. (2020). Reflected protons in the lunar wake and their effects on wake potentials. *Journal of Geophysical Research: Space Physics*, *125*, e2020JA028154. https://doi.org/10.1029/2020JA028154

Received 23 APR 2020
Accepted 21 MAY 2020
Accepted article online 7 JUN 2020

Abstract The refilling of the lunar wake is facilitated by the wake ambipolar electric potential arising from the electron pressure gradient. Incident solar wind protons can be reflected by the lunar crustal magnetic fields and the lunar surface on the dayside and repicked up, entering the lunar wake due to their large gyroradii. This burst of positive charges can cause the lunar wake potential to be reduced by hundreds of volts. We utilize over 7 years of ARTEMIS (Acceleration, Reconnection, Turbulence, and Electrodynamics of the Moon's Interaction with the Sun) measurements to systematically investigate how the reflected protons affect the lunar wake potential structure when the Moon is immersed in the solar wind. RPs have a peak occurrence rate of ~20% for downstream distances from the Moon at $N \times 2\pi R_g$ and a preference of high occurrence rates and high densities in the direction of the motional electric field of the solar wind. We show that reflected protons in the lunar wake can significantly change the electrostatic ambipolar potentials in the wake, leading in turn to the formation of field-aligned, accelerated electron beams. Our case study also suggests a nonmonotonic field-aligned potential structure in the presence of reflected protons in the wake. Lastly, our results show that when the reflected proton density is larger than ~30% of the local proton density from refilling solar wind protons, the wake potential scales as the logarithmic density of reflected protons, which can be explained by the Boltzmann relation.

1. Introduction

The terrestrial Moon is a physical obstacle to the solar wind plasma flow and can be approximated as an airless and unmagnetized body to first order (e.g., Colburn et al., 1967; Ness et al., 1968; Russell et al., 2016). The lunar wake is thus a nearly complete plasma void immediately downstream from the nightside hemisphere of the Moon due to the removal of solar wind ions and electrons on the dayside. The refilling of the wake by the supersonic solar wind flow is facilitated by the wake ambipolar electric potential, formed by electron pressure gradients along the interplanetary magnetic field (IMF) lines. Many studies have provided analytical solutions for this refilling process theorized with different assumptions (e.g., Halekas et al., 2014; Hutchinson, 2012; Samir et al., 1983; Ogilvie et al., 1994; Xu et al., 2019), mainly built on the 1-D plasma expansion theory by Gurevich et al. (1969) and Gurevich and Pitaevskii (1975).

The Moon possesses small-scale crustal magnetic fields dispersed widely across its surface with sizes ranging from less than one to thousands of kilometers and magnitudes up to at least hundreds of nanotesla at the surface (e.g., Halekas et al., 2001; Hood & Schubert, 1980; Mitchell et al., 2008; Purucker & Nicholas, 2010). Despite small scales, these crustal magnetic fields can reflect incident solar wind protons from the dayside hemisphere of the Moon (e.g., Futaana et al., 2003; Lue et al., 2011; Poppe et al., 2017; Saito et al., 2008), locally reducing the space weathering rates on the lunar regolith (e.g., Hood & Williams, 1989). Incident solar wind protons can also be reflected by the lunar surface, though its flux is much smaller than the reflected protons by crustal fields. These reflected protons are "repicked up" and can enter the wake because of their large gyroradii. Reflected protons entering the wake can cause disturbances to the equilibrium state of the lunar wake (e.g., Dhanya et al., 2016; Nishino et al., 2013). In particular, Nishino et al. (2013) suggested that these reflected protons in the deep wake could cause outward-pointed electric fields (opposite direction to the ambipolar electric field from the refilling process), which would accelerate electrons inward to maintain charge neutrality. This is consistent with reduced wake potentials on the order of 100 V coincident with reflected proton observations in the wake as shown in a case study by Xu et al. (2019) (their Figure 3).

In order to systematically investigate reflected protons' properties in the lunar wake and their effects on the lunar wake potential, we utilize more than 7 years of ARTEMIS (Acceleration, Reconnection, Turbulence, and Electrodynamics of the Moon's Interaction with the Sun) observations to conduct statistical analyses. In section 2, we describe the ARTEMIS instrumentation, how to separate reflected protons from solar wind protons, and how to obtain wake potentials. In section 3, we present our main results, including a case study, statistical analyses on reflected protons in the wake, and their effects on the wake potential. We then conclude our paper in section 4.

2. Methodology

The ARTEMIS mission consists of two probes, P1 and P2, orbiting the terrestrial Moon in elliptical orbits, which used to be Probes B and C of the Time History of Events and Macroscale Interactions during Substorms (THEMIS) mission. Each spacecraft carries a comprehensive suite of plasma and field instruments (Angelopoulos, 2011) and started collecting measurements in the lunar plasma environment in mid-2011. In this study, we use electron and ion data from the Electro-Static Analyzer (ESA) (McFadden et al., 2008) and vector magnetic fields measured by the fluxgate magnetometer (FGM) (Auster et al., 2008) from both probes from June 2011 to the end of 2018.

The region of interest of this study is when the terrestrial Moon is immersed in the solar wind, upstream of Earth's bow shock. Similar to Xu et al. (2019), we select data when the Moon is located upstream of Earth's bow shock, which is identified by a bow shock fit (Chao et al., 2002) with its nose placed at 15 R_e, in lieu of 13 R_e, to account for bow shock movements. We calculate upstream solar wind conditions, including the solar wind velocity, density, and IMF magnitude and direction, separately for the inbound and outbound legs of each lunar wake crossing by averaging the upstream parameters just prior to and just after entry and exit from the lunar wake for $r_{cyl} = [1,1.5]R_L$, where r_{cyl} is the cylindrical distance from the X axis.

To investigate reflected protons in the lunar wake, we first need to separate them from the solar wind bulk flow. This is achieved by assuming the solar wind flow is within a cone of 45° in solid angle in the antisolar direction and also a spread in energy within 0.25–4 times of the peak solar wind proton energy, shortened as "SWP" hereafter. Ions in other look directions within this energy range and in all look directions outside of this energy range are considered to be reflected protons, shortened as "RP" hereafter. There are a few caveats with such assumptions: (1) This energy range might not capture all the solar wind flow when solar wind protons are hot, and (2) RP can occasionally be in the antisunward direction too with solar wind proton energies, which will be counted as SWP. In addition, there are lunar pick-up ions of exospheric origin, most of which are heavier than protons, yet would be classified as RPs by our methodology. However, because of their larger gyroradii than reflected protons, these pick-up ions are less likely to enter the deep lunar wake (e.g., Halekas et al., 2012; Halekas, Poppe, Delory et al., 2013). Terrestrial foreshock ions can also enter the lunar wake, and we have not filtered them out, as our results suggest this source is a minor contribution compared to reflected protons in the wake.

Additionally, we filtered out a small set of times (approximately $< 10\%$ of all measurements) when the ARTEMIS ground software algorithms incorrectly transformed the spacecraft spin angle into the standard Solar-Selenocentric-Ecliptic (SSE) coordinate frame, which causes SWP to appear to be in the wrong look direction and to be classified as RP (e.g., ~18:24 UT in Figures 1d–1f). The SSE coordinates are defined as the X axis points from the center of the Moon to the Sun, the Z axis points to ecliptic north, and the Y axis completes the right-handed system. To minimize this misidentification, we impose a limit on the ratio of the RP density to the upstream solar wind density to be less than 10% for our statistical analyses. Furthermore, as the RP density is usually small, instrument background removal becomes important. We calculate background count rates from the averaged count rates for ion energies < 30 eV (where the solar wind proton fluxes should be nonexistent) and subtract this count rate, corrected for different angular bin sizes, from all energy and angular bins before converting to fluxes and moments for each measurement. After this background subtraction, we impose a minimum density threshold of 3σ to identify a valid (statistically significant) RP detection, where σ is the standard deviation of non-SWP densities outside of the wake ($r_{cyl} = [1,1.5]R_L$).

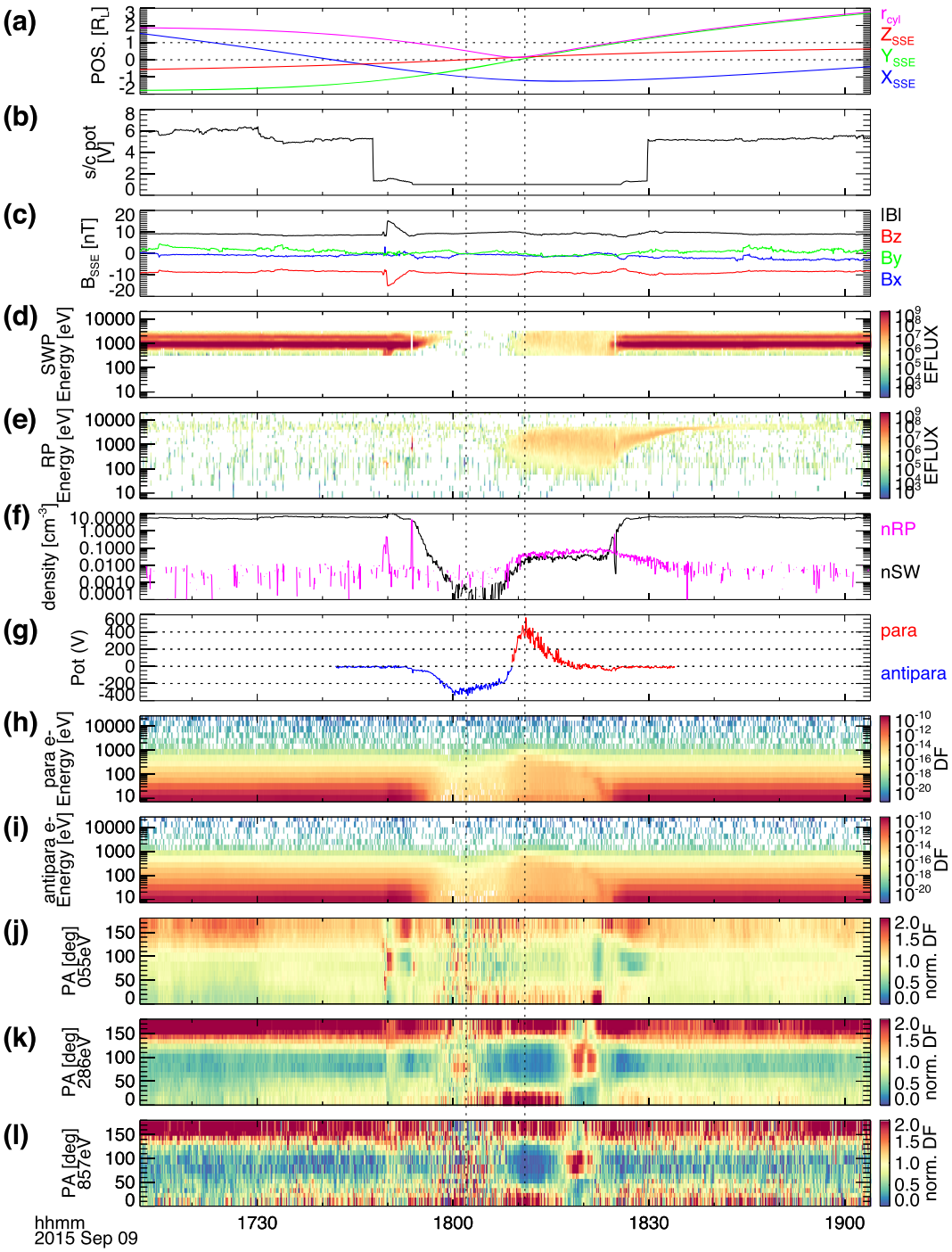

Figure 1. An orbit example of the ARTEMIS Probe P1 on 9 September 2015. From top to bottom, the time series of (a) the spacecraft position in the SSE coordinates and r_{cyl} is the distance from the X axis; (b) the spacecraft potential; (c) the magnetic field strength and vector components in the SSE coordinates; the averaged ion energy spectra for solar wind protons (d) and reflected protons (e); (f) the calculated ion density for solar wind protons (blue) and reflected protons (red); (g) the deduced wake potential from electrons traveling toward the wake, blue for parallel electrons and red for antiparallel electrons; (h) and (i) the electron phase space density [cm^{-3} $(km/s)^{-3}$] for pitch angles (PAs) 0–15° and 165–180° , respectively; and (j–l) normalized pitch angle distributions for energy bins centered at 55, 286, and 857 eV, respectively. The vertical dotted lines mark where electron spectra in Figure 2 are taken.

Finally, the lunar wake potential is obtained using the methodology previously described in Halekas et al. (2011) and Xu et al. (2019), by comparing the distribution function of field-aligned electrons traveling into the wake to that in the upstream solar wind. Specifically, the wake potential is calculated as the averaged

energy shift between these two types of electrons for energies 40–500 eV, assuming the zero potential to be outside of the wake. To better handle positive potentials that may occur in the presence of RPs, when the phase space density (PSD) for 400–1,000 eV electrons in the wake is higher than that in the upstream solar wind, an energy range of 100–1,000 eV is used instead to calculate the potential to avoid averaging negative and positive energy shifts (see an example in section 3.1). This is done for each inbound and outbound wake-crossing segment separately from late 2011 to the end of 2018.

3. Results

3.1. Example Observations

We start with an example observation to illustrate that reflected protons in the lunar wake can change the wake potential by hundreds of volts. Figure 1 shows the observation from P1 on 9 September 2015. The spacecraft entered the lunar wake at ~17:54 UT (universal time) and exited at ~18:24 UT (Figure 1a). For this wake crossing, the upstream IMF is mostly steady, mainly in the $-Z_{SSE}$ direction. In the wake, the solar wind proton flux shown in Figure 1d decreases significantly, as expected, corresponding to a decrease of SWP density up to 3 orders of magnitude (the black line in Figure 1f). In comparison, a significant RP flux is seen in Figure 1e inside the wake, as well as outside. It is possible that the flux outside the wake is partially attributed to lunar exospheric pick-up ions. The RP density (the magenta line in Figure 1f) ranges from ~0.001 to ~0.1 cm^{-3} inside the wake from 18:08 to 18:34 UT. Coincident with the high RP flux, there is a local enhancement in the low SWP flux and density in the deep wake (18:08 to 18:23 UT) seen in Figures 1d and 1f, which is most likely RPs in the antisunward direction that are miscategorized as SWP.

For the inbound segment, the derived wake potential (the red line in Figure 1g, after correction with the spacecraft potentials in Figure 1b, is ~0 V outside of the wake and decreases deeper into the wake to approximately −300 V at 18:00 UT, as expected (Xu et al., 2019). In contrast, for the outbound segment, entering the wake, the wake potentials (the blue line in Figure 1g) decreases from 0 to −50 V at ~18:22 UT but then becomes mostly positive, with a peak of greater than +400 V at ~18:11 UT. Positive wake potentials occur at the location where the local RP density surpasses the local SWP density, as seen in Figure 1f. This is not unexpected: When there is a burst of positive charges in the wake, comparable to or higher than the local density, to preserve charge neutrality, the potential is shortened, or an outward electric field is formed (Nishino et al., 2013), to accelerate electrons into the wake. Correspondingly, electron pitch angle distributions for energies above 200 eV (Figures 1k and 1l) become beamed along both the parallel and antiparallel directions (18:08–18:16 UT). In contrast, electron pitch angle distributions for periods without RP (e.g., 17:54–18:00 UT) resemble that in the upstream (e.g., 17:40–17:50 UT), with a strong beaming at PA 150–180° due to the solar wind strahl electrons. Similar counterstreaming electron observations concurring with reflected protons in the lunar wake were reported by Nishino et al. (2013).

To better understand electrons' behavior in the wake for periods with and without RP, we show the electron PSD distribution for parallel, perpendicular, and antiparallel pitch angles for 18:02 UT (a) and 18:11 UT (b) in Figure 2. At 18:02 UT (Figure 2a), in the absence of RPs, the maximum PSD for electrons in the wake (solid lines) is much smaller than that of upstream solar wind electrons (dashed lines), as low-energy solar wind electrons are filtered/reflected by a negative wake potential. The energy shift from antiparallel electrons (traveling toward the wake) allows us to infer a wake potential of approximately −250 V. In contrast, at 18:11 UT (Figure 2b), both the parallel and antiparallel electrons in the wake are shifted to higher energies than those in the upstream solar wind for energies above 100 eV. The semi-flattop distribution below ~400 eV in both parallel and antiparallel directions is also an indicator of electrons going through a field-aligned acceleration by an electrostatic potential comparable to the edge of the flattop. The high PSD below 30 eV likely results from secondary electrons produced within the instrument due to impact ionization by high energy electrons. A few observations can be made for this example. (1) The maximum PSD (above 30 eV) for electrons within the wake is much smaller than that in the upstream, indicating these electrons first experience a negative wake potential that filters out low-energy electrons. By comparing this maximum PSD to the upstream electron distribution function, we can infer a wake potential of approximately −100 V. (2) Electrons in the wake are shifted to higher energies than that in the solar wind at energies above 100 eV, indicating a positive wake potential. The energy shift from parallel electrons gives a wake potential of +400 V. Note that this energy shift should be obtained with energies >100 eV in order to exclude false

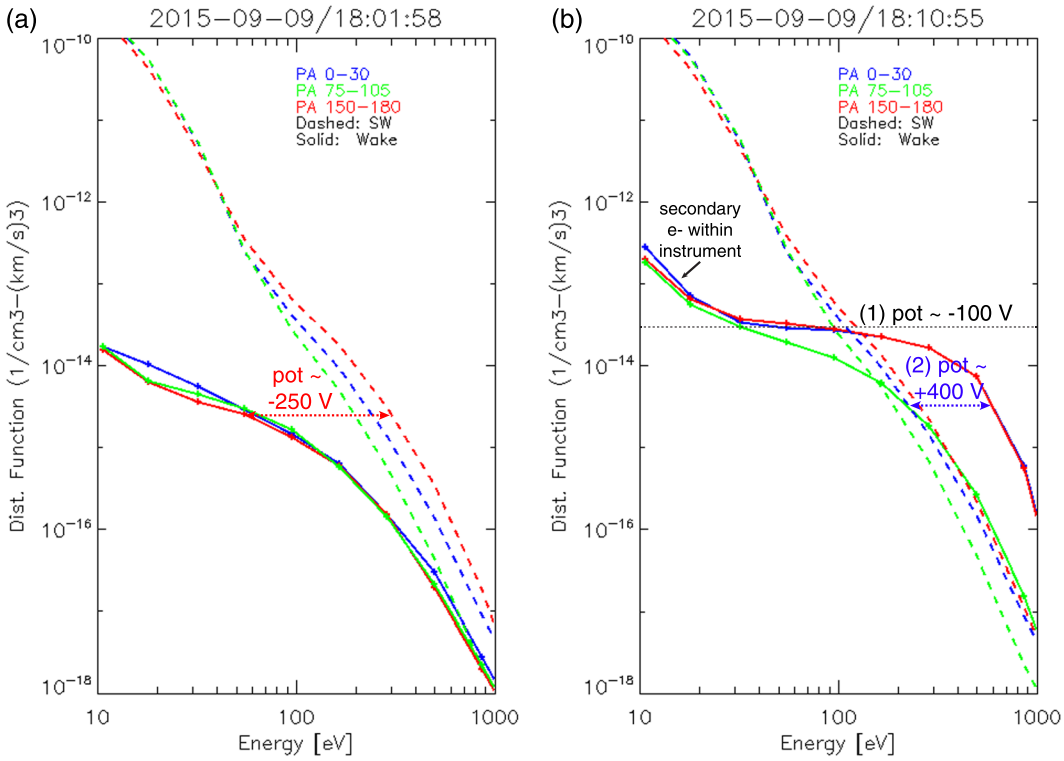

Figure 2. The electron phase space density [cm^{-3} $(km/s)^{-3}$] against energy for pitch angles 0–30° (blue), 75–105° (green), and 150–180° (red) for 18:02 UT (a) and 18:11 UT (b), as indicated by the two dotted dashed line in Figure 1. In each panel, the dashed lines are for upstream solar wind electrons and the solid lines for electrons in the wake.

negative energy shifts at the low energies. (3) The perpendicular electrons (the green spectrum) are accelerated to a different energy, compared to field-aligned electrons. It might be because these electrons have different sources, starting at different locations, as they pass through the wake at different time scales with different parallel velocities, although a deeper study of this behavior is left for future work.

The case study in Figure 2b suggests these electrons have experienced a nonmonotonic field-aligned potential structure, first decelerated by a potential approximately −100 V and then accelerated by a potential of +400 V. Note that wake potentials in Figure 1g are probably on different field lines, representing the potential difference between the spacecraft and the upstream, and should thus not be taken as the potential structure along a single field line. Instead, we can infer the potential structure along each individual field line by comparing the distributions of local electrons and upstream electrons. Also, since field-aligned superthermal electrons can traverse the wake within seconds (100 eV ~ 6,000 km/s), it is more likely this nonmonotonic potential structure is spatial rather than temporal. More often than not, when RPs are present in the wake, we find a nonmonotonic field-aligned potential structure. For this specific example in Figure 2b, the expected wake potential without RPs is probably approximately −200 to −300 V (Figure 1g), but we obtain a potential of +400 V instead. This means that the presence of RPs in the wake has probably altered the wake potential up to 600–700 V. Lastly, during this time period, significant low-frequency (< 1,000 Hz) waves are detected (not shown here) by the electric field instrument (EFI) (Bonnell et al., 2009) in the presence of RPs in the wake (e.g., Tao et al., 2012).

3.2. Statistical Ensemble of Reflected Protons in the Lunar Wake

The case study above shows that when the RP density in the wake is comparable to or higher than the local SWP density, the negative lunar wake potential can be significantly reduced and driven to large positive values. To systematically investigate RP's properties in the wake and their effects on the wake potential, we collect ARTEMIS data from late 2011 to the end of 2018 and confine our data to be when the Moon is in the solar wind with the method described in section 2. We also confine our data selection to periods

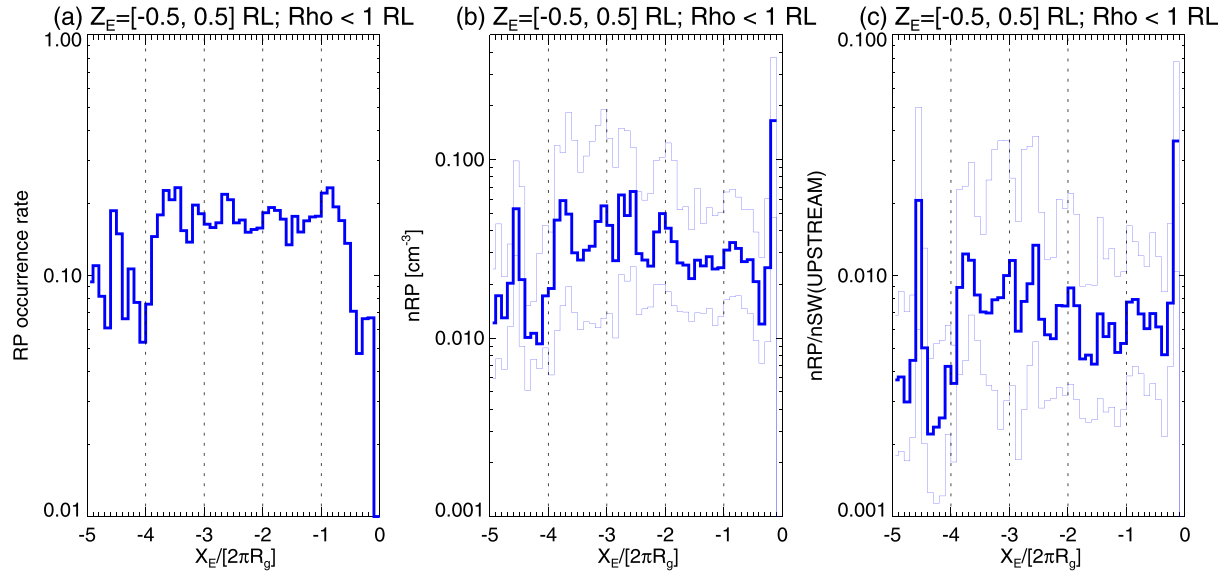

Figure 3. The occurrence rate (a), the median density (b), and the median density ratio to the upstream solar wind density (c) for reflected protons as a function of $X_E/(2\pi R_g)$, where R_g is the proton gyroradius, for $r_{cyl} < 1R_L$ and $|Z_E| < 0.5R_L$. The thin lines in (b) and (c) are quartiles.

with relatively steady IMF conditions such that the wake is not highly perturbed, defined as conditions where the cone angle (relative to the X axis) varies within $< 60°$ and the clock angle (arctan(B_{ZSSE}/B_{YSSE})) varies within $< 90°$ for inbound and outbound segments just outside the lunar wake. Reflected protons are also expected to show a preference in the positive motional electric field direction from the solar wind, that is, $-\mathbf{V}\times\mathbf{B}$, where $\mathbf{V}$ is the solar wind velocity vector and $\mathbf{B}$ is the IMF vector. We rotate the frame to such a coordinate system, where the X axis (X_E) is antiparallel to the solar wind flow, the Z axis (Z_E) is in the direction of $-\mathbf{V}\times\mathbf{B}$, and the Y axis (Y_E) completes the right-handed system.

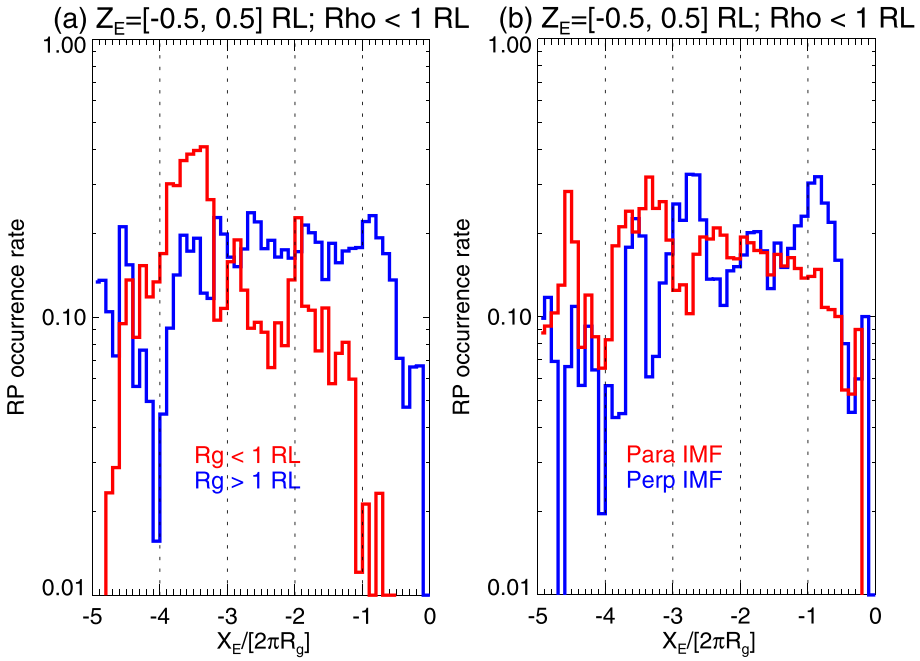

Figure 4. The occurrence rate of reflected protons as a function of $X_E/(2\pi R_g)$ for $r_{cyl} < 1R_L$ and $|Z_E| < 0.5R_L$, separated for different conditions. (a) The blue line is the RP occurrence rate for $R_g > 1R_L$ and red for $R_g < 1R_L$. (b) The blue line is the RP occurrence rate for more perpendicular IMFs ($60° <$ cone angle $< 120°$) and red for more parallel IMFs (cone angle $< 60°$ or $> 120°$).

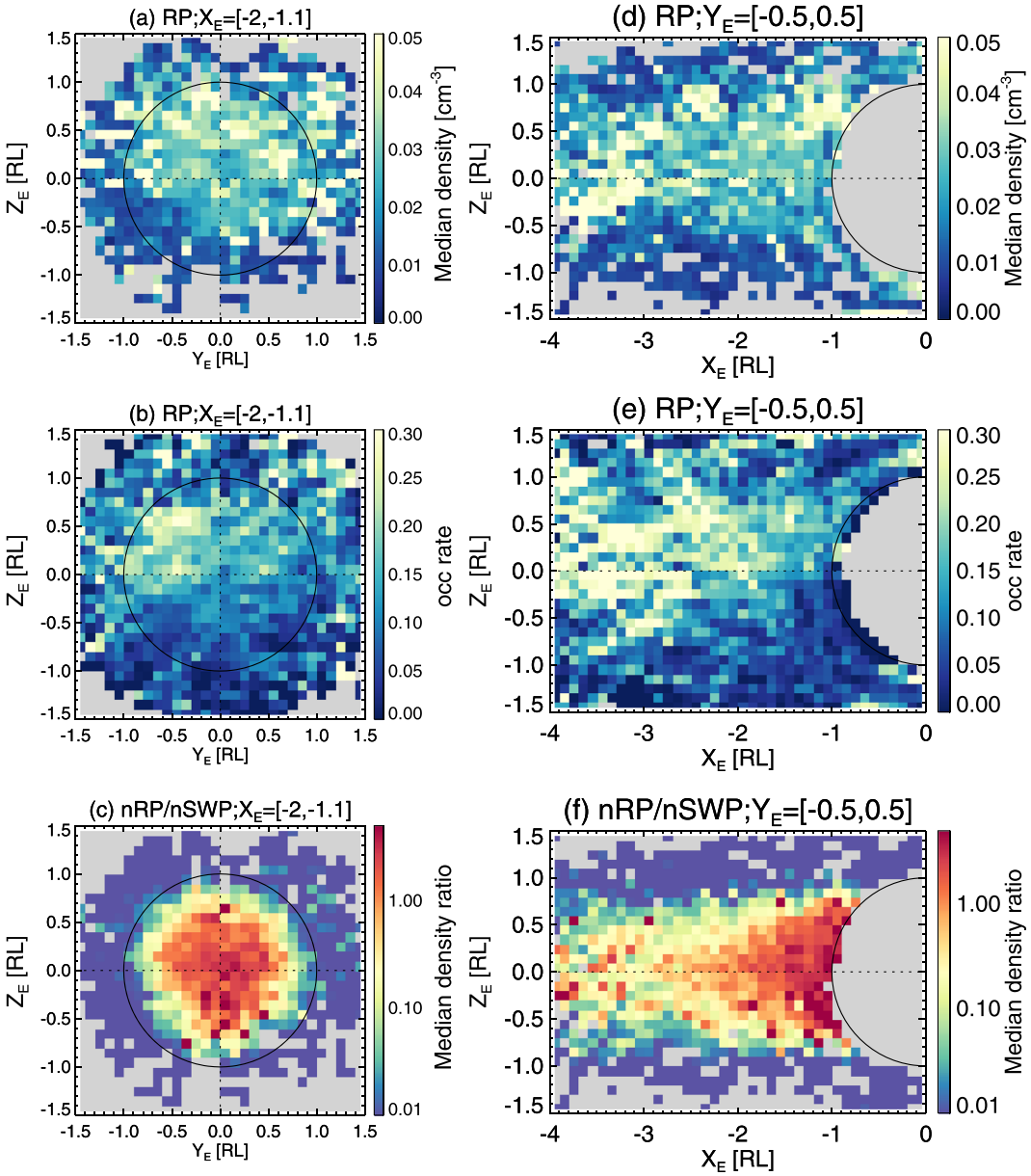

Figure 5. The occurrence rate (a and d), the median density (cm^{-3}) (b and e), and the median density ratio to the local solar wind density (c and f) for reflected protons in different projections. The left column is in the Y_E-Z_E plane for $X_E = [-2.0,-1.1]R_L$ and the right in the X_E-Z_E plane for $Y_E = [-0.5,-0.5]R_L$.

To demonstrate that our method of separating RP from SWP is effective, we calculate the occurrence rate of RP, the median RP density, and the median ratio of RP density to the upstream solar wind density as a function of the proton gyroradius along X_E for $r_{cyl} < 1R_L$ and $|Z_E| < 0.5R_L$, shown in Figure 3. The typical proton gyroradius is close to the lunar radius, 2,221 km for a solar wind velocity of 400 km/s, a Parker spiral angle of 45°, and an IMF strength of 8 nT. The occurrence rate peaks at 20% near N times of $2\pi R_g$ in Figure 3a, as expected, where R_g is the proton gyroradius. There are a few possible reasons for not exactly peaking at $N \times 2\pi R_g$: (1) protons lose energy as they gyrate further downstream so that their gyroradii become smaller than what is estimated with the solar wind velocity; (2) the location where protons are reflected on the Moon is not necessarily at the subsolar region so that the starting point can be anywhere from 0–1 R_L; and (3) the magnetic field strength increases slightly in the wake than that in the upstream (e.g., Poppe et al., 2014; Zhang et al., 2014), which would cause the gyroradius to decrease too. The median RP density is

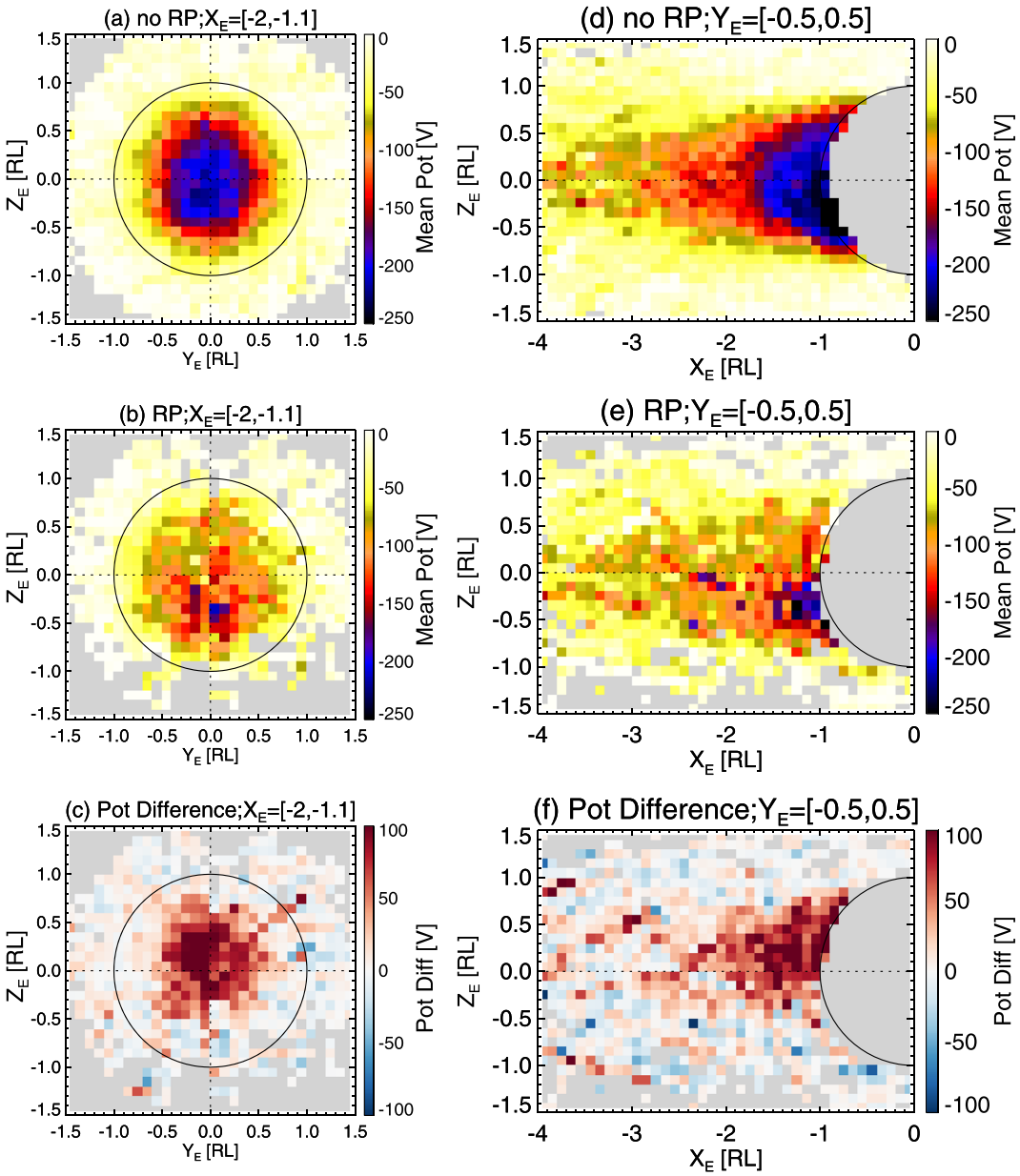

Figure 6. The averaged wake potentials in the Y_E-Z_E plane for $X_E = [-2.0,-1.1]R_L$ (a and b) and the right in the X_E-Z_E plane for $Y_E = [-0.5,-0.5]R_L$ (d and e). The upper row is for when there is no reflected proton and the lower row for when there are reflected protons. The potential differences of these two scenarios, that is, averaged potentials in Figures 6b–6e subtracted by averaged potentials in Figures 6a–6d, are shown in Figures 6c and 6f, respectively.

~0.05 cm^{-3} in Figure 3b, and the density of RPs with respect to the upstream solar wind density is ~1% in Figure 3c. The RP density and relative density both also have peaks near $N \times 2\pi R_g$, though slightly less clear than the occurrence rate.

We further examine the behavior of reflected protons in the wake for different conditions: the proton gyroradius and the IMF cone angle. Figure 4a shows the comparison of the occurrence rate of RPs for $R_g > 1R_L$ (blue) and $R_g < 1R_L$ (red). For $R_g < 1R_L$, reflected protons have a higher chance to impact back to the Moon within their first gyration, resulting into a negligible occurrence rate for $-1 < X_E/(2\pi R_g) < 0$. In contrast, the occurrence rates shows an even peaking at $N \times 2\pi R_g$ for larger gyroradii. Figure 4b compares the RP occurrence rate for more perpendicular IMFs (60° < cone angle < 120°, blue) and for more parallel IMFs

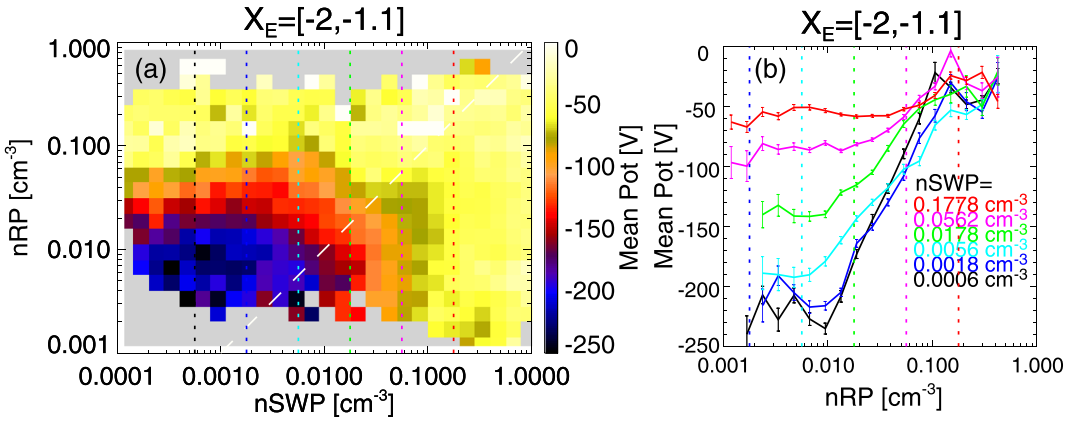

Figure 7. (a) The mean wake potentials as a function of the local solar wind density and the reflected proton density for $X_{SSE} = [-2.0,-1.1]R_L$. The dashed white line marks the 1-to-1 ratio. (b) The mean wake potentials as a function of the reflected proton density, different colors for different local solar wind densities, with error bars indicate errors to the mean values. The vertical dotted lines in both (a) and (b) mark the logarithmic mean values of each local SWP density range.

(cone angle $< 60°$ or $>120°$, red). For more parallel IMFs, the occurrence rate is lower for $-1 < X_E/(2\pi R_g) < 0$ and does not peak as clearly at $N \times 2\pi R_g$ as perpendicular IMFs. The IMF cone angle affects RPs' behavior in multiple ways. For more parallel IMFs, R_g tends to be smaller, as the perpendicular velocity is smaller. In addition, the structure of $N \times 2\pi R_g$ is probably more smeared out for more parallel fields, because these ions are convected off to the side of the wake as they gyrate downstream around the magnetic field (e.g., Fatemi et al., 2014). Lastly, protons tend to be reflected completely upstream for parallel IMF (e.g., Halekas, Poppe, McFadden, et al., 2013) such that they do not appear in the wake at all. Therefore, there are clearer peaks at $N \times 2\pi R_g$ for more perpendicular IMFs, but it is a more smeared out structure for more parallel IMFs.

To examine the asymmetry in the behavior of the RPs as a function of the motional electric fields from the solar wind, we show the mapping of the RP's properties in Figure 5 in the Y_E-Z_E plane for $X_E = [-2.0,-1.1]$ R_L (a–c) and in the X_E-Z_E plane for $Y_E = [-0.5,0.5]R_L$ (e and f). There is a clear asymmetry between the $\pm Z_E$ sectors in both the occurrence rate (Figures 3a and 3d) and the density (Figures 3b and 3e), higher toward the $+Z_E$ direction, as expected. This again validates our method of separating RP from SWP. The median RP density in the wake is ~0.04 cm^{-3}, and the occurrence rate is 20–30% for $Z_E > -0.5R_L$. The density ratio of RP to the local SWP increases from < 0.01 outside of the wake to >1 in the deep wake, indicating a significant disturbance of RP when the local SWP density is small. High-density ratios are also concentrated to a smaller cylindrical radius in the $-Z_E$ sector than that in the $+Z_E$ sector, as shown in Figure 5c.

3.3. Reflected Protons' Effects on Wake Potentials

As shown above, the RPs in the wake can be a significant disturbance locally and are thus expected to alter wake potentials as shown in the case study. The averaged wake potentials for when there is no RP in the wake are shown in Figures 6a and 6d and for detectable RPs in Figures 6b and 6e. The potential differences of these two scenarios, that is, averaged potentials in Figures 6b and 6e subtracted by averaged potentials in Figures 6a and 6d, are shown in Figures 6c and 6f, respectively. The wake potentials are similar at the edge of the wake for both scenarios (~0.6 R_L from the center) but differ by up to >100 V in the deep wake. Large potential differences occur in regions with large local RP-to-SWP density ratios, as shown in Figures 5c and 5f. There is also a clear $\pm Z_E$ asymmetry in the potential difference, corresponding to the asymmetry in the presence of RPs in the wake (Figure 5).

To more quantitatively examine the effects of RPs on wake potentials, Figure 7a shows the mean wake potentials as a function of the local SWP density and the local RP density for $X_E = [-2.0,-1.1]R_L$. The wake potential becomes more negative for smaller local SWP density (Xu et al., 2019), which approximately indicates how deep in the wake the measurement is. When the local RP density is less than the local SWP density (the lower right half below the white dashed line), that is, a small local disturbance, the wake potential is roughly constant for a particular local SWP density. In contrast, the wake potential becomes less negative

with increasing local RP density for a fixed SWP density above the white dashed line due to the significant local disturbance by RPs.

Another way to illustrate the trend is to plot the wake potential against the RP density for a small range of the local SWP densities, highlighted in different colors in Figure 7b. The wake potential is roughly constant when the RP density (n_{RP}) is less than ~30% of the local SWP density (n_{SWP}), as the local disturbance is small. In contrast, for conditions when $n_{RP}/n_{SWP} >$ ~30%, the wake potential scales logarithmically with the RP density. When the RP density entirely surpasses the local SWP density, for example, the black and blue lines in Figure 7b, the wake potential changes similarly for these two cases as a function of n_{RP}, as now n_{RP} is the dominant species, statistically speaking.

4. Discussion and Conclusions

In this study, we separate RP from SWP in the lunar wake with ARTEMIS measurements by assuming SWP to be in a cone of 45° and an energy range of 0.25–4 times of the peak upstream solar wind proton energy. By utilizing ARTEMIS data from late 2011 to the end of 2018, we conduct statistical analyses on RP's properties in the lunar wake when the Moon is immersed in the solar wind. RPs have a peak occurrence rate of ~20% for downstream distances from the Moon at $N \times 2\pi R_g$ and a preference of high occurrence rates and high densities in the direction of the motional electric field of the solar wind. These results validate our methodology to separate these two proton populations. The median RP density is ~0.05 cm^{-3} and the relative density to the upstream solar wind ~1%. We also find that the occurrence rate is negligible within RPs' first gyration when their gyroradii are small, as they are more likely to impact back to the Moon. Furthermore, there are clearer peaks at $N \times 2\pi R_g$ for more perpendicular IMFs, but it is a more smeared out structure for more parallel IMFs for the aforementioned reasons.

Our case study shows that the electrostatic ambipolar potential in the wake can be altered by a burst of high RP flux up by >600 V, even resulting in positive wake potentials. When RPs locally reduce the wake potential, electrons are accelerated by the outward-pointing electric fields, resulting in counterstreaming, field-aligned pitch angle distributions. More interestingly, by comparing electrons in the wake with upstream electrons, we infer a nonmonotonic potential structure along the field line for the first time because of the presence of RPs. Our case study suggests that this nonmonotonic potential field-aligned structure first decelerates electrons by approximately −100 eV and then accelerates them to a final state of gaining approximately +400 eV.

Statistically, the reduction in the wake potential due to the presence of RPs is about 100 V on average and occurs mostly in the deep wake. This is because RP densities are generally small, a few tenths percent of the upstream solar wind density, but can be a significant local disturbance in the deep wake where local SWP densities are also small. Quantitatively, the wake potential is found to scale as the logarithm of the RP density for when $n_{RP}/n_{SWP} >$ ~30%. This logarithmic linear, or semilogarithmic, relation can be explained by the Boltzmann relation, $-\nabla(nT_e) = en\nabla\varphi$, THAT IS, the balance of the plasma pressure gradient and electric terms, where n is the plasma density, φ is the potential, and T_e is the electron temperature in energy units. With the presence of RPs, particularly with a nonmonotonic field-aligned potential structure, the simple 1-D plasma expansion theory may no longer be applicable but rather requires more sophisticated numerical models to simulate the state of the lunar wake.

It is interesting that the averaged potentials rarely pass +0 V in Figures 6 and 7, yet a positive potential of +400 V is obtained for the case study with a moderate local RP density < 0.1 cm^{-3} (Figure 1). This +400 V potential may be an extreme case whereby significant additional fluxes of RPs are present farther along the magnetic field line where ARTEMIS cannot measure them (i.e., since the ARTEMIS probe is cutting across individual field lines in this example) such that this large positive potential is an accumulated result. This is not an unreasonable assumption as a relatively high flux of RPs is continuously measured over 10 min in our case study. This type of event with RPs dominating over a large spatial volume probably does not occur frequently such that any large positive potentials may be smeared out in the statistical results.

Finally, our understanding of perturbations to the lunar wake potential structure by reflected protons has implications for observations of magnetospheric interactions with other airless satellites throughout the solar system. For example, simulations of Rhea's magnetospheric interaction performed by Roussos et al.

(2008) suggested that exospheric pick-up ions from Rhea's thin exosphere may gyrate into Rhea's wake at close downstream distances. In turn, the perturbations to the lunar wake potential seen here in ARTEMIS observations may indicate that similar processes are occurring at Rhea and, by extension, other Saturnian satellites.

Data Availability Statement

All ARTEMIS data necessary for this study are publicly available online (at http://artemis.ssl.berkeley.edu). Data access and processing were done using SPEDAS V3.1; see Angelopoulos et al. (2019).

Acknowledgments

S. X., A. R. P., and J. S. H. gratefully acknowledge support from NASA's Solar System Exploration Research Virtual Institute (SSERVI), grants #NNX14AG16A and #NNX15AH15A. A. R. P. and S. X. also acknowledge support from NASA's Lunar Data Analysis Program, Grant #80NSSC18K1565. The ARTEMIS mission is funded and operated under NASA Grant NAS5-02099, and we specifically acknowledge K.-H. Glassmeier, U. Auster, and W. Baumjohann for the use of FGM data provided under the lead of the Technical University of Braunschweig and with financial support through the German Ministry for Economy and Technology and the German Center for Aviation and Space (DLR), Contract 50 OC 0302.

References

Angelopoulos, V. (2011). The ARTEMIS mission. *Space Science Reviews*, *165*, 3–25. https://doi.org/10.1007/s11214-010-9687-2

Angelopoulos, V., Cruce, P., Drozdov, A., Grimes, E., Hatzigeorgiu, N., King, D., et al. (2019). The Space Physics Environment Data Analysis System (SPEDAS). *Space Science Reviews*, *215*(1), 9.

Auster, H., Glassmeier, K., Magnes, W., Aydogar, O., Baumjohann, W., Constantinescu, D., et al.(2008). The THEMIS fluxgate magnetometer. *Space Science Reviews*, *141*(1-4), 235–264.

Bonnell, J., Mozer, F., Delory, G., Hull, A., Ergun, R., Cully, C., et al. (2009). The electric field instrument (EFI) for THEMIS, *The THEMIS mission* (pp. 303–341). New York, NY: Springer.

Chao J., Wu, D., Lin, C.-H., Yang, Y.-H., Wang, X., Kessel, M., et al. (2002). Models for the size and shape of the Earth's magnetopause and bow shock. *Cospar Colloquia series* (Vol.12, pp. 127–135). Pergamon: Elsevier.

Colburn, D. S., Currie, R. G., Mihalov, J. D., & Sonett, C. P. (1967). Diamagnetic solar-wind cavity discovered behind Moon. *Science*, *158*(3804), 1040–1042.

Dhanya, M., Bhardwaj, A., Futaana, Y., Barabash, S., Alok, A., Wieser, M., et al. (2016). Characteristics of proton velocity distribution functions in the near-lunar wake from Chandrayaan-1/SWIM observations. *Icarus*, *271*, 120–130.

Fatemi, S., Holmström, M., Futaana, Y., Lue, C., Collier, M. R., Barabash, S., & Stenberg, G. (2014). Effects of protons reflected by lunar crustal magnetic fields on the global lunar plasma environment. *Journal of Geophysical Research: Space Physics*, *119*, 6095–6105. https://doi.org/10.1002/2014JA019900

Futaana, Y., Machida, S., Saito, Y., Matsuoka, A., & Hayakawa, H. (2003). Moon-related nonthermal ions observed by Nozomi: Species, sources, and generation mechanisms. *Journal of Geophysical Research: Space Physics*, *108*(A1), 1025. https://doi.org/10.1029/2002JA009366

Gurevich, A., & Pitaevskii, L. (1975). Non-linear dynamics of a rarefied ionized gas. *Progress in Aerospace Sciences*, *16*, 227–272.

Gurevich, A. V., Pitaevskii, L., & Smirnova, V. (1969). Ionospheric aerodynamics. *Space Science Reviews*, *9*(6), 805–871.

Halekas, J., Angelopoulos, V., Sibeck, D., Khurana, K., Russell, C., Delory, G., et al. (2011). First results from ARTEMIS, a new two-spacecraft lunar mission: Counter-streaming plasma populations in the lunar wake. *The ARTEMIS Mission* (pp. 93–107). New York, NY: Springer.

Halekas, J., Mitchell, D., Lin, R., Frey, S., Hood, L., Acuña, M., & Binder, A. (2001). Mapping of crustal magnetic anomalies on the lunar near side by the lunar prospector electron reflectometer. *Journal of Geophysical Research*, *106*, 27,841–27,852. https://doi.org/10.1029/2000JE001380

Halekas, J. S., Poppe, A., Delory, G., Sarantos, M., Farrell, W., Angelopoulos, V., & McFadden, J. (2012). Lunar pickup ions observed by ARTEMIS: Spatial and temporal distribution and constraints on species and source locations. *Journal of Geophysical Research*, *117*, E06006. https://doi.org/10.1029/2012JE004107

Halekas, J., Poppe, A., Delory, G., Sarantos, M., & McFadden, J. (2013). Using ARTEMIS pickup ion observations to place constraints on the lunar atmosphere. *Journal of Geophysical Research: Planets*, *118*, 81–88. https://doi.org/10.1029/2012JE004292

Halekas, J., Poppe, A., & McFadden, J. (2014). The effects of solar wind velocity distributions on the refilling of the lunar wake: ARTEMIS observations and comparisons to one-dimensional theory. *Journal of Geophysical Research: Space Physics*, *119*, 5133–5149. https://doi.org/10.1002/2014JA020083

Halekas, J., Poppe, A., McFadden, J., & Glassmeier, K.-H. (2013). The effects of reflected protons on the plasma environment of the Moon for parallel interplanetary magnetic fields. *Geophysical Research Letters*, *40*, 4544–4548. https://doi.org/10.1002/grl.50892

Hood, L., & Schubert, G. (1980). Lunar magnetic anomalies and surface optical properties. *Science*, *208*(4439), 49–51.

Hood, L., & Williams, C. (1989). *The lunar swirls-Distribution and possible origins, in Lunar and Planetary Science Conference Proceedings*, vol. 19, pp. 99–113.

Hutchinson, I. (2012). Electron velocity distribution instability in magnetized plasma wakes and artificial electron mass. *Journal of Geophysical Research*, *117*, A03101. https://doi.org/10.1029/2011JA017119

Lue, C., Futaana, Y., Barabash, S., Wieser, M., Holmström, M., Bhardwaj, A., et al. (2011). Strong influence of lunar crustal fields on the solar wind flow. *Geophysical Research Letters*, *38*, L03202. https://doi.org/10.1029/2010GL046215

McFadden, J., Carlson, C., Larson, D., Ludlam, M., Abiad, R., Elliott, B., et al. (2008). The THEMIS ESA plasma instrument and in-flight calibration. *Space Science Reviews*, *141*(1-4), 277–302.

Mitchell, D., Halekas, J., Lin, R., Frey, S., Hood, L., Acuña, M., & Binder, A. (2008). Global mapping of lunar crustal magnetic fields by lunar prospector. *Icarus*, *194*(2), 401–409.

Ness, N. F., Behannon, K. W., Taylor, H. E., & Whang, Y. C. (1968). Perturbations of the interplanetary magnetic field by the lunar wake. *Journal of Geophysical Research*, *73*(11), 3421–3440.

Nishino, M. N., Fujimoto, M., Saito, Y., Tsunakawa, H., Kasahara, Y., Kawamura, M., et al. (2013). Type-II entry of solar wind protons into the lunar wake: Effects of magnetic connection to the night-side surface. *Planetary and Space Science*, *87*, 106–114.

Ogilvie, K. W., Steinberg, J. T., Fitzenreiter, R. J., Owen, C. J., Lazarus, A. J., Farrell, W. M., & Torbert, R. B. (1994). Observations of the lunar plasma wake from the WIND spacecraft on December 27. *Geophysical Research Letters*, *23*, 1255–1258. https://doi.org/10.1029/96GL01069

Poppe, A., Fatemi, S., Halekas, J., Holmström, M., & Delory, G. (2014). ARTEMIS, observations of extreme diamagnetic fields in the lunar wake. *Geophysical Research Letters*, *41*, 3766–3773. https://doi.org/10.1002/2014GL060280

Poppe, A., Halekas, J., Lue, C., & Fatemi, S. (2017). ARTEMIS Observations Of the solar wind proton scattering function from lunar crustal magnetic anomalies. *Journal of Geophysical Research: Planets*, *122*, 771–783. https://doi.org/10.1002/2017JE005313

Purucker, M. E., & Nicholas, J. B. (2010). Global spherical harmonic models of the internal magnetic field of the moon based on sequential and coestimation approaches. *Journal of Geophysical Research*, *115*, E12007. https://doi.org/10.1029/2010JE003650

Roussos, E., Wuller, J., & Simon, S. (2008). Plasma and fields in the wake of Rhea: 3-D hybrid simulation and comparison with Cassini data. In *Annales geophysicae: atmospheres, hydrospheres and space sciences*. (Vol. 26, p. 619).

Russell, C. T., Luhmann, J. G., & Strangeway, R. J. (2016). Space physics: An introduction, Cambridge University Press.

Saito, Y., Yokota, S., Tanaka, T., Asamura, K., Nishino, M., Fujimoto, M., et al. (2008). Solar wind proton reflection at the lunar surface: Low energy ion measurement by MAP-PACE onboard SELENE (KAGUYA). *Geophysical Research Letters*, *35*, L24205. https://doi.org/10.1029/2008GL036077

Samir, U., Wright, Jr. K., & Stone, N. H. (1983). The expansion of a plasma into a vacuum: Basic phenomena and processes and applications to space plasma physics. *Reviews of Geophysics*, *21*(7), 1631–1646.

Tao, J., Ergun, R., Newman, D., Halekas, J., Andersson, L., Angelopoulos, V., et al. (2012). Kinetic instabilities in the lunar wake: ARTEMIS observations. *Journal of Geophysical Research*, *117*, A03106. https://doi.org/10.1029/2011JA017364

Xu, S., Poppe, A. R., Halekas, J. S., Mitchell, D. L., McFadden, J. P., & Harada, Y. (2019). Mapping the lunar wake potential structure with ARTEMIS data. *Journal of Geophysical Research: Space Physics*, *124*, 3360–3377. https://doi.org/10.1029/2019JA026536

Zhang, H., Khurana, K., Kivelson, M., Angelopoulos, V., Wan, W., Liu, L., et al. (2014). Three-dimensional lunar wake reconstructed from ARTEMIS data. *Journal of Geophysical Research: Space Physics*, *119*, 5220–5243. https://doi.org/10.1002/2014JA020111